Petroleum Science 19 (2022) 2081–2094

Contents lists available at ScienceDirect

Petroleum Science

journal homepage: www.keaipublishing.com/en/journals/petroleum-science

Original Paper

A computational method for wide-azimuth 3D dip-angle gathers using Gaussian beam migration

Su-Bin Zhuang [a], Jian-Ping Huang [a, *], Ji-Dong Yang [a], Zhen-Chun Li [a]

[a] School of Geosciences, China University of Petroleum (East China), Qingdao, 266580, Shandong, China

ARTICLE INFO

Article history:
Received 2 April 2021
Accepted 25 November 2021
Available online 14 March 2022

Edited by Jie Hao

Keywords:
Gaussian beam
Dip-angle gathers
3D imaging
Diffraction

ABSTRACT

The dip-angle-domain common-image gather (DDCIG) is a key tool to separate the diffraction and reflection imaging results. Reflectors with different spatial geometries produce different responses in DDCIGs. Compared with Kirchhoff migration, Gaussian beam migration (GBM) is more effective and robust to overcome the multipathing problem. As a ray-based method, it has explicit angle information naturally during the propagation. We have developed a 3D DDCIG computational method using GBM, which obtain both the imaging result and angle-domain gathers with only one pass of calculation. The angle-gather computation is based on geometrical optics, and multiple angle conversions are implemented under the rules of space geometry, which helps to avoid rounding errors and improve accuracy. Additionally, the multi-azimuth joint presentation strategy is proposed to describe the characteristic of omnidirectional dip angles using a finite number of gathers. After using a 2D model to illustrate application advantages of DDCIG, we apply the proposed method to two 3D models to test its feasibility and accuracy. A field data example further demonstrates the adaptability of our method to seismic imaging for a land survey.

1. Introduction

Up to date, seismic migration has been widely used in oil and gas exploration, geotechnical engineering, civil engineering and other industrial fields. Common migration methods can be categorized into two groups: ray-based and wave-equation-based migrations. As one of the major ray-based migration methods, Kirchhoff migration has high efficiency. But it also has some limitations such as caustics, shadow and multipathing problems (Popov, 1982, 2002; Babich and Popov, 1989; Bleistein, 1999; Hill, 2001; Gray et al., 2002; Liu and Palacharla, 2011). By contrast, wave-equation-based migration, such as reverse-time migration, has higher imaging accuracy. However, Yang et al. (2015a) noted the limited industrial application of the method because of the vast amount of memory consumed during the calculation process and the low computational efficiency due to the multiple calculations of the full wavefield.

In recent years, Gaussian beam migration (GBM) has come under renewed interest because of its relatively good calculation efficiency and accuracy (Kachalov and Popov, 1981; Červený et al., 1982; Popov, 1982; Červený, 1983a). Ever since the basic framework of GBM was first proposed by Hill (1990, 2001), the implementation of GBM has been mainly divided into two schemes based on traveltime and wavefield.

Traveltime-based GBM depends mainly on the time relationship of Gaussian beams from the source and receiver, after which the amplitude of each imaging point can be calculated. Nowack et al. (2003) and Gray (2005) improved Hill's method by introducing the local slant stack strategy, which makes it suitable for common shot and common receiver gathers. Furthermore, Yue et al. (2012) and Huang et al. (2016) proposed local elevation static correction and effective neighborhood wavefield approximation to achieve true-amplitude migration of the complex surface. In the area with anisotropy, Alkhalifah (1995) improved GBM in anisotropic media according to the anisotropic ray tracing system proposed by Červený (1972). In addition, after supplementing and modification of this GBM method by Zhu et al. (2007), Duan et al. (2013) and Han et al. (2014), a lot of advancements in the technique of anisotropic imaging are noted. Technological advancement has triggered rapid development of various types of seismic beam migration at the same time. For example, Nowack (2008, 2011) introduced the idea of deep focusing to the Gaussian beam theory and developed methods for focused beam migration and dynamic focused beam migration. Yang et al. (2015b) optimized the propagation of seismic

* Corresponding author.
E-mail address: jphuang@upc.edu.cn (J.-P. Huang).

https://doi.org/10.1016/j.petsci.2022.03.012

beams based on Fresnel body ray tracing, and proposed a prestack Fresnel beam migration method. On the other hand, wavefield-based GBM depends on the Gaussian beam propagation operator to describe the forward-propagated and backward-propagated seismic wavefields. The final image can be achieved according to the imaging condition applied. Typical methods such as Gaussian packet migration proposed by Žáček (2004, 2006) can achieve accurate target-oriented imaging. Geng et al. (2011, 2014) improved the representation of Gaussian packet in the observed wavefield and the modified packet not only reduces the redundancy of Gabor basis function, but also improves the calculation efficiency. Furthermore, Shi et al. (2016) stacked Delta packet to represent Green's function in the time domain. On the basis of it, Yang et al. (2018b) and Yue et al. (2019a, 2019b, 2020, 2021a, 2021b) applied the linear forward modeling technique and developed a time-domain least squares Gaussian beam migration method. In general, although wavefield-based GBM gives better results compared to traveltime-based GBM, it requires frequent inverse Fourier transform during the calculation, which is very time-consuming.

GBM has numerous advantages including its ability to provide a physical interpretation of seismic wave propagation into the subsurface, making it easier to describe wave phenomena in complex geophysical models (Gray and Bleistein, 2009). This technique is also powerful in imaging steeply inclined layers because ray tracing methods are independent of the imaging angle. On the other hand, Gaussian beam method is very efficient and suitable for imaging massive field data. Most importantly, it uses complex-valued initial beam parameters for dynamic ray tracing, which can avoid the problem of singular amplitude near the caustics. The local plane wave decomposition in different directions allows it to propagate independently from different directions to the underground imaging point, so the multipathing problem is completely solved. (Hale, 1992b; Yang et al., 2018a).

The key property of the GBM is that its operator directly contains ray angles during the migration. Therefore, Gaussian beam method can be used to extract angle-domain gathers conveniently and quickly. In contrast, when reverse time migration is needed to represent the relationship between angles of the local space, a three-dimensional Poynting vector containing angle information must be additionally calculated and perform a series of variable substitutions (Thomas and Graham, 2011; Jiang et al., 2017; Kwangjin, 2017; Liu et al., 2017). This undoubtedly increases calculation cost due to a huge amount of calculation performed.

The common-image gather (CIG) contains the velocity and lithology information of the underground media, which is usually used for velocity analysis and amplitude versus offset (AVO) analysis (Gray, 2007). The shot-domain common-image gather (SDCIG) and the offset-domain common-image gather (ODCIG) are the most widely-used CIGs due to its simple principle and realizability (Nolan and Symes, 1996). However, when the multi-wave arrival phenomenon is intense, it generates virtual values in migration unavoidably, especially in regions of high lateral velocity contrast (Huang and Fehler, 2000). To overcome this situation, Xu et al. (2001) proposed to extract gathers in the opening angle domain which can provide favorable support for amplitude versus angle (AVA) analysis and lithology analysis (Cai et al., 2013). However, the imaging response curve of the reflection layer and the diffraction point is similar, which is hard to distinguish or separate the diffraction and reflection energy. This defect can be fixed by dip-angle-domain common-image gathers (DDCIGs). (Brandsberg-Dahl et al., 2003; Ursin, 2004). The DDCIGs can separate the scattering-angle information from reflection layers, which can not only improve the signal-to-noise ratio of the final gather, but also have great significance for the study of separation and imaging of diffraction wave (Kong et al., 2016). Thus, DDCIG is gradually becoming one of the most important and commonly used gathers in the field data processing.

In recent years, wide-azimuth 3D seismic exploration has gradually become the mainstream (Yao et al., 2019, 2020). Under this general trend, we try to extract DDCIGs in the wide-azimuth 3D media based on Gaussian beam prestack depth migration. In this paper, we first review the principle of GBM, and then analyze the angle relationship in 3D local space near the imaging point in detail. Based on the geometric theory, we derive two extraction formulas of GBM-based DDCIGs. Finally, typical numerical examples and the field data processing results demonstrate the validity and adaptability of the proposed method.

2. Theory

In this section, we will first briefly review the principle of Gaussian beam prestack depth migration, and then analyze the geometric relationship between the vectors in the local three-dimensional space near the imaging point. Finally, we will introduce two formulas for extracting the dip-angle-domain common-image gathers (DDCIGs) based on the three-dimensional Gaussian beam propagation vector.

2.1. Review of Gaussian beam prestack depth migration in 3D medium

According to Červený and Pšenčík (1983b, 1983c, 1984), Gaussian beam in the 3D ray-centered coordinates has the following expression:

$$u_{GB}(s,m,n;\omega)=\sqrt{\frac{v(s)\det\mathbf{Q}(s_0)}{v(s_0)\det\mathbf{Q}(s)}}\exp\left\{i\omega\left[t_0+\int_{s_0}^{s}\frac{ds}{v(s)}\right]+\frac{i\omega}{2}\mathbf{q}^{T}\mathbf{P}\mathbf{Q}^{-1}\mathbf{q}\right\}, \quad (1)$$

where (s, m, n) represent 3D ray-centered coordinates (see Fig. 1); ω is the circular frequency; $v(s)$ and $v(s_0)$ mean the velocity along the

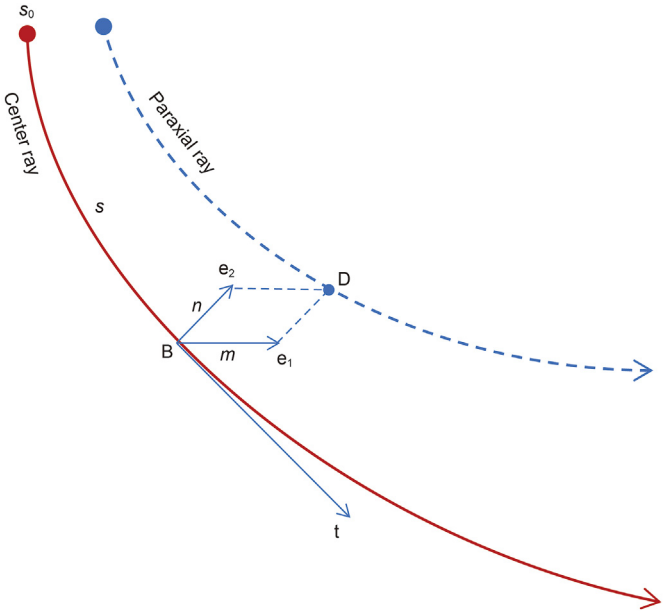

Fig. 1. 3D ray-centered coordinates. The base vector is **t**, $\mathbf{e_1}$, and $\mathbf{e_2}$, and the corresponding base coordinates are (s, m, n).

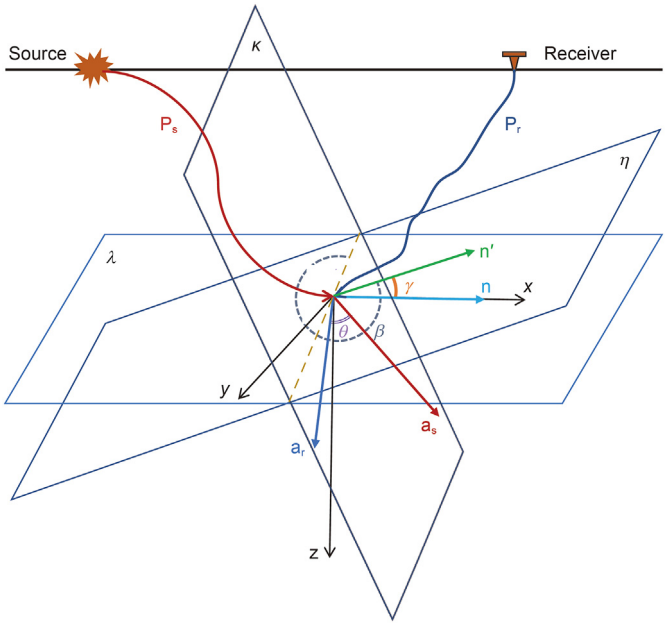

Fig. 2. Illustration of 3D local space. The vector $\mathbf{P_s}$ and $\mathbf{P_r}$ represent ray vectors of the downward wavefield from the source and the reverse wavefield from the receiver; $\mathbf{a_s}$ and $\mathbf{a_r}$ are their unit representation; the symbol θ represents the reflection angle and the symbol β represents the azimuth; symbols λ, η, and κ represent the horizontal plane, reflection plane, and common plane, respectively; the vector $\mathbf{n}$ and $\mathbf{n}'$ are the reference vector and its projection on the plane η

central raypath and at the beginning of the ray, respectively; **P** and **Q** are the complex-valued solutions of dynamic ray-tracing equations and kinematic ray-tracing equations, which determine the wavefront curvature and the beam width in a form of a 2 × 2 complex matrix (Popov, 2002; Červený, 2005).

The function $u_{GB}(s,m,n;\omega)$ in Eq. (1) represents the local wavefield, which is composed of one single beam taking off from the point source in 3D space. However, we can build Green's function to describe its global wavefield by integrating over all takeoff angles as shown in Eq. (2):

$$G_r(\mathbf{x},\mathbf{x_r};\omega)=\frac{i\omega}{2\pi}\int_{p_{xm}}^{p_{xn}}\int_{p_{ym}}^{p_{yn}}u_{GB}(\mathbf{x},\mathbf{x_r};\omega)\frac{dp_y dp_x}{p_z},$$
$$G_s(\mathbf{x},\mathbf{x_s};\omega)=\frac{i\omega}{2\pi}\int_{p_{xm}}^{p_{xn}}\int_{p_{ym}}^{p_{yn}}u_{GB}(\mathbf{x},\mathbf{x_s};\omega)\frac{dp_y dp_x}{p_z}, \quad (2)$$

where $G_r(\mathbf{x},\mathbf{x_r};\omega)$ and $G_s(\mathbf{x},\mathbf{x_s};\omega)$ represent Green's function from the receiver and source points ($\mathbf{x_r}$ and $\mathbf{x_s}$) respectively; p_{xm}, p_{xn} and p_{ym}, p_{yn} are the minimum and maximum values of ray parameters in x and y directions. To improve the accuracy while maintaining computational efficiency, Hill (1990) and Yue et al. (2012) added a phase and an amplitude correction factor into Eq. (2) respectively. The factors mentioned above correct for changes in the phase and amplitude caused by the differences in the near-surface velocity gradient and elevation. This increases the accuracy level and doesn't affect the overall calculation efficiency. On the other hand, we follow Hill's prestack imaging idea that Gaussian beam migration can be extended to prestack migration by using the updown imaging principle (Claerbout, 1970; Hill, 2001).

Based on this principle, Zhang et al. (2007) achieved pre-stack migration by using the correlation-type imaging condition with Gaussian Beam:

$$I(\mathbf{x})=\int\frac{2\pi v(\mathbf{x})}{i\omega}P_{up}(\mathbf{x},\mathbf{x_s};\omega)P^*_{down}(\mathbf{x},\mathbf{x_s};\omega)d\omega, \quad (3)$$

where $P_{up}(\mathbf{x};\mathbf{x_s};\omega)$ and $P_{down}(\mathbf{x};\mathbf{x_s};\omega)$ represent the upgoing (recorded) and the downgoing (source) wavefields, and * denotes complex conjugation. These two wavefields are the key to imaging, which can be represented with the help of the Green's function in Eq. (2). Here, we refer to the pre-stack migration formula proposed by Hill (2001):

$$I(\mathbf{x})=\frac{-1}{2\pi}\int d\omega\iint dx_r dy_r\iint dx_s dy_s\frac{\partial G^*_r(\mathbf{x},\mathbf{x_r};\omega)}{\partial z_r}G^*_s(\mathbf{x},\mathbf{x_s};\omega)R(\mathbf{x_r},\mathbf{x_s};\omega), \quad (4)$$

where $G_r(\mathbf{x},\mathbf{x_r};\omega)$ and $G_s(\mathbf{x},\mathbf{x_s};\omega)$ are the beam representations of Green's function introduced in Eq. (2); $R(\mathbf{x_r},\mathbf{x_s};\omega)$ denotes seismic records received at geophones.

According to Eqs. (1), (2) and (4) above, we can get the final imaging value at any point underground in 3D medium with Gaussian beam.

2.2. Geometric relationship in 3D local space

From the perspective of geometric seismology, if the incident ray occurs from the source to the position where the upper wave impedance differs from the lower wave impedance, it will inevitably produce the corresponding reflected ray, which satisfies Snell's law (see Fig. 2). Without considering the interference of the converted wave, the transmitted rays that are generated simultaneously with the reflection can be regarded as the continuous propagation of source energy.

After considering the ray theory and the wavefield continuation in GBM, we construct the Cartesian coordinates in a three-dimensional local space as shown in Fig. 2. Undoubtedly, if a point underground can be imaged, $\mathbf{P_s}$ and $\mathbf{P_r}$ must be a pair of vectors with physical existence used together for illumination. Based on this, we construct $\mathbf{P_s}$ and $\mathbf{P_r}$ at a random location underground. As shown in Fig. 2, the reflection angle (θ) is the angle between two vectors of $\mathbf{P_s}$ and $\mathbf{P_r}$. So its formula can be written as

$$\cos(\theta)=\frac{\mathbf{P_s}\cdot\mathbf{P_r}}{|\mathbf{P_s}|\cdot|\mathbf{P_r}|}=\mathbf{a_s}\cdot\mathbf{a_r}, \quad (5)$$

where the numerator is the scalar product of two vectors, and the denominator is the product of two vector modules. After simplification, it is the scalar product of two unit ray vectors. If half of the reflection opening angle ($\theta/2$) is combined with the depth as two dimensions to form a gather, we call it angle-domain common-image gather (ADCIG). Obviously, there are multiple ADCIGs at the same location in 3D space, which represent different directions. These ADCIGs are not the same due to the different quality of the ray illumination under different azimuths. The same situation applies to DDCIG.

Before studying the azimuth that is a key parameter in DDCIG, we need to first set $\mathbf{n}$ = (1, 0, 0) as the reference direction (see Fig. 2). By referring to the law of light reflection in physical optics, we know that the incident ray, the reflected ray, and the normal line are coplanar. We call it the common plane κ. The reflection plane which is perpendicular to plane κ is called plane η and the horizontal plane is named as λ (see Fig. 2). With the help of the reference vector $\mathbf{n}$, the azimuth (β) can be represented mathematically. It is the angle between the vector $\mathbf{n}'$ which is the projection of the reference vector $\mathbf{n}$ on the plane η, and the intersection vector of plane κ and plane η (see Fig. 2).

It should be mentioned that the value of β in the omnidirectional observation system ranges from 0° to 360°, so the sine function and cosine function need to be used in combination to uniquely determine the true value of the azimuth. The formula of the azimuth is given below, and the detailed derivation is discussed in Appendix 1:

$$\mathbf{a} = \mathbf{a_s} + \mathbf{a_r}, \tag{6}$$

$$\sin(\beta) = \frac{(\mathbf{a_s} \times \mathbf{a_r}) \times (\mathbf{n} \times \mathbf{a}) \cdot \mathbf{a}}{|\mathbf{a_s} \times \mathbf{a_r}| \cdot |\mathbf{n} \times \mathbf{a}| \cdot |\mathbf{a}|}, \tag{7}$$

$$\cos(\beta) = \frac{(\mathbf{n} \times \mathbf{a}) \cdot (\mathbf{a_s} \times \mathbf{a_r})}{|\mathbf{n} \times \mathbf{a}| \cdot |\mathbf{a_s} \times \mathbf{a_r}|}, \tag{8}$$

where all the parameters have been mentioned before.

The dip angle (γ) of the reflection plane is the plane angle of the dihedral angle formed by the reflection plane η and the horizontal plane λ (see Fig. 2). Fig. 3 (most of parameters correspond to those in Fig. 2) can be viewed as a front view of the common plane κ in Fig. 2, that is, the paper surface can be regarded as the above-mentioned plane κ. This paper shows two solutions to represent γ in direct method and indirect method.

First, a direct method for the computation of two side vectors that form the angle γ is formulated. The vector $\mathbf{x'} = [\cos(\beta), \sin(\beta), 0]$ (see Fig. 3) can be determined by constructing the intersection of the horizontal plane λ and the common plane κ (see Fig. 2), where β represents the azimuth. From principles of isosceles triangle in the plane geometry, $\mathbf{a'} = \mathbf{a_s} - \mathbf{a_r}$ (see Fig. 3) is exactly perpendicular to the normal line, which is parallel to the inclined plane in Fig. 3. After determining the two side vectors, the expression of angle γ can be written as follows:

$$\cos(\gamma) = \mathrm{sign}(\gamma) \cdot \frac{\mathbf{x'} \cdot (\mathbf{a_s} - \mathbf{a_r})}{|\mathbf{a_s} - \mathbf{a_r}|}, \tag{9}$$

$$\mathrm{sign}(\gamma) = \begin{cases} 1 & , \quad (\mathbf{a_s} - \mathbf{a_r}) \cdot \mathbf{m} < 0 \\ -1 & , \quad (\mathbf{a_s} - \mathbf{a_r}) \cdot \mathbf{m} > 0 \end{cases}, \tag{10}$$

where $\mathbf{m} = (0, 0, 1)$ is the vertical downward unit vector in the three-dimensional Cartesian coordinates, as shown in Fig. 3. The direct method calculates γ directly, which is intuitive and easy to understand. However, the azimuth β is introduced in the calculation step. During the computation stage, unavoidable round-off error arise which lowers the calculation accuracy.

In order to avoid calculation defects of the direct method, we derive a formula of the indirect method by finding an angle which is equal to the dip angle to perform the transformation. As shown in Fig. 3, with the help of two parallel lines, a pair of alternate interior angles are equal in size. At the same time, with the help of two vertical relationships, two angles that are mutually complementary to the common angle are equal. Therefore, the angle formed by two vectors $\mathbf{a}$ and $\mathbf{m}$ is equal to the dip angle of the reflection plane. Then the formula of indirect method can be written as

$$\cos(\gamma) = \mathrm{sign}(\gamma) \cdot \frac{\mathbf{m} \cdot (\mathbf{a_s} + \mathbf{a_r})}{|\mathbf{a_s} + \mathbf{a_r}|}, \tag{11}$$

$$\mathrm{sign}(\gamma) = \begin{cases} 1 & , \quad (\mathbf{a_s} + \mathbf{a_r}) \cdot \mathbf{x'} > 0 \\ -1 & , \quad (\mathbf{a_s} + \mathbf{a_r}) \cdot \mathbf{x'} < 0 \end{cases}, \tag{12}$$

where all the parameters have been mentioned before. It should be noted that the range of dip angle in Eq. (9) is still from 0° to 180°, but in Eq. (11) it is from 0° to −90° and from 90° to 0°, as the reflection plane η goes from flat to vertical and then back to flat (see Fig. 4). Finally, after modification, it can be organized into from −90° to 90° with the help of Eqs. (10) and (12).

2.3. Calculation of ray parameters based on 3D Gaussian beam

The geometric relationship of three-dimensional local space near the imaging point has been analyzed and derived in detail before. The problem to be considered at present is to calculate two initial ray vectors $\mathbf{P_s}$ and $\mathbf{P_r}$.

Equation (1) is the expression of Gaussian beam in the 3D ray-centered coordinates. As its basic form is a plane harmonic wave, we can view it as two parts. The part before the exponent is the initial amplitude, which represents the initial energy of the beam. The part inside the exponent is the complex time-term, which

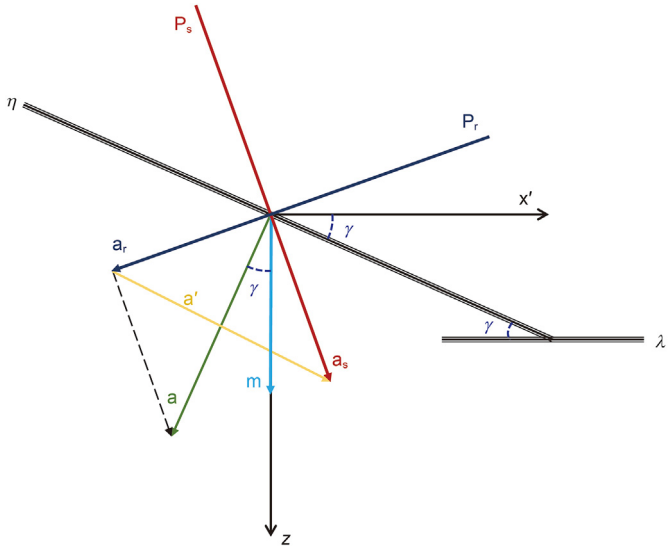

Fig. 3. 2D local coordinate system in the common plane. The symbol γ represents the dip angle.

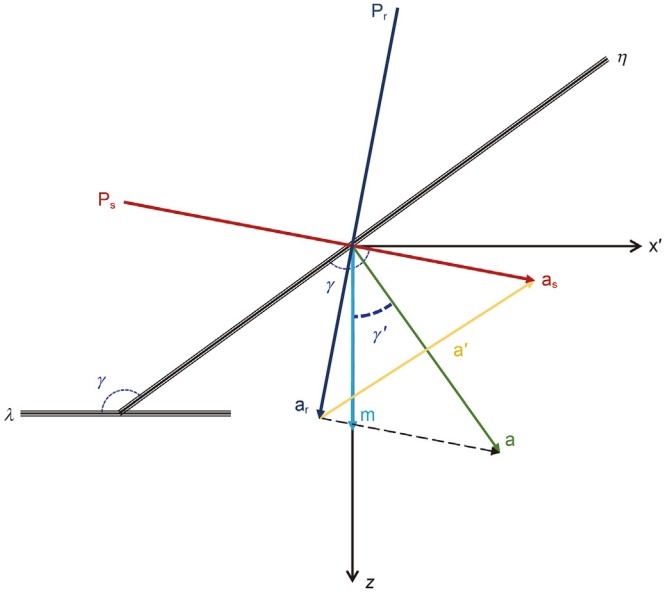

Fig. 4. 2D local coordinate system in the common plane (the second case).

determines the amplitude decay and phase change resulting from the propagation. We expand the time-term and analyze it in detail:

$$t = t_0 + \int_{s_0}^{s} \frac{\mathrm{d}s}{v(s)} + \frac{1}{2}\mathbf{q}^{\mathrm{T}}\mathrm{Re}\left(\mathbf{P}\mathbf{Q}^{-1}\right)\mathbf{q} = \tau(s) + \frac{1}{2}\mathbf{q}^{\mathrm{T}}\mathrm{Re}\left(\mathbf{P}\mathbf{Q}^{-1}\right)\mathbf{q}, \tag{13}$$

where t represents the time from the beginning to any point on the beam; t_0 is the initial time which covers the response delay of the geophone in the actual exploration. The second term is an integral. It represents the ray propagation time from the beginning to the nearest point on the center ray to the target; $\mathbf{q}^{\mathrm{T}}\mathbf{P}\mathbf{Q}^{-1}\mathbf{q}/2$ means the time of transition from the central ray to the paraxial ray (see Fig. 1).

After calculating the traveltime of any point underground, we can get the slowness vector by calculating the space derivatives of three base vectors in the Cartesian coordinates:

$$p_k = \frac{\partial T}{\partial x_k} \quad ; k = 1, 2, 3\,, \tag{14}$$

where $k = 1, 2, 3$ means three directions of the coordinate system. Inserting Eq. (13) into Eq. (14), we can get the following formula:-

$$p_k(D) = p_k(\mathrm{B}) + m\frac{\partial m}{\partial x_k}M_{11} + n\frac{\partial n}{\partial x_k}M_{22} + \frac{1}{2}\left(m\frac{\partial n}{\partial x_k} + n\frac{\partial m}{\partial x_k}\right)(M_{12} + M_{21}) \quad ; k = 1, 2, 3\,, \tag{15}$$

where the point D and B are shown in Fig. 1; m and n are components of two directions in the 3D ray-centered coordinates and $\mathbf{q} = (m, n)^{\mathrm{T}}$; $\mathbf{M} = \mathbf{P}\mathbf{Q}^{-1}$ is a 2×2 matrix:

$$\mathrm{Re}(\mathbf{M}) = \mathrm{Re}\left(\mathbf{P}\mathbf{Q}^{-1}\right) = \begin{pmatrix} M_{11} & M_{12} \\ M_{21} & M_{22} \end{pmatrix}. \tag{16}$$

Based on Eq. (15), three components can be solved in turn to construct a complete three-dimensional slowness vector. According to properties of the slowness vector and the ray parameter equivalent, the solution of ray parameters based on Gaussian beam can be realized.

3. Numerical examples

In this section, we first study the characteristics of the dip-angle-domain common-image gathers (DDCIGs) in a 2D model. Then, based on the above theory and algorithm, we select two 3D models to test the performance of 3D DDCIGs. To further study the flexibility and robustness of the extraction method in this paper, we apply the new method to land field data from eastern China.

We start with a numerical example to investigate the application advantages of DDCIGs. As shown in Fig. 5a, the model consists of a horizontal layer with constant velocity and four pairs of symmetrically slanted layers with different dip angles. Moreover, the profile of the model is radial like light, so we name it the light model. At the beginning, we use a staggered-grid finite-difference method in the numerical simulation to get seismic records. The accuracy in space and time are eighth order and second order, respectively. The main frequency is 20 Hz. In addition, a total of 201 shots are simulated with a shot interval of 40 m from the beginning to the end at the surface. Concurrently, 201 geophones are set up at intervals of 40 m. The recording time is 2 s, and the time sampling interval is 2 ms.

Considering the fact that ray tracing requires the second derivative of velocity, Gaussian filtering to the velocity model in

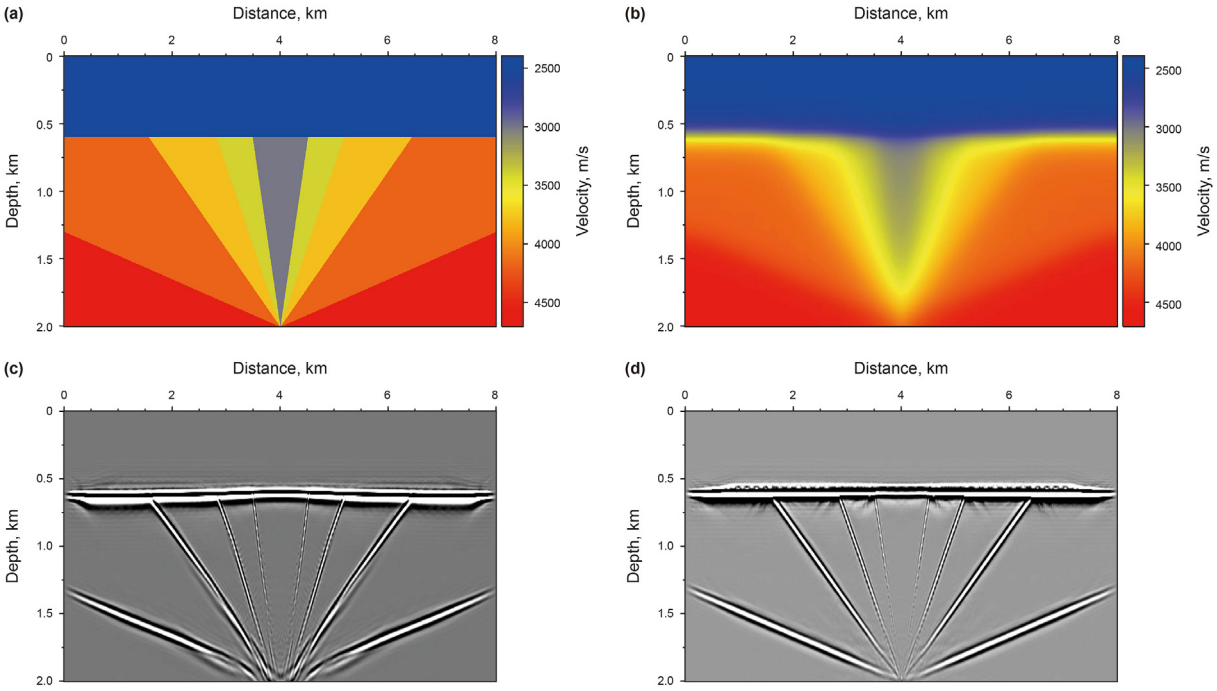

Fig. 5. The light model and its migration result: (**a**) velocity model, (**b**) smoothed velocity model, (**c**) Kirchhoff prestack depth migration result, (**d**) Gaussian beam prestack depth migration result.

Fig. 5a is applied. Linear smoothing of the model is carried out to ensure the stability in subsequent calculation of dynamic ray tracing (Popov et al., 2010). Finally, the background velocity (see Fig. 5b) and seismic records obtained are incorporated into the calculation framework of GBM. This yields an accurate image as shown in Fig. 5d. It is worth noting that Gaussian beam method

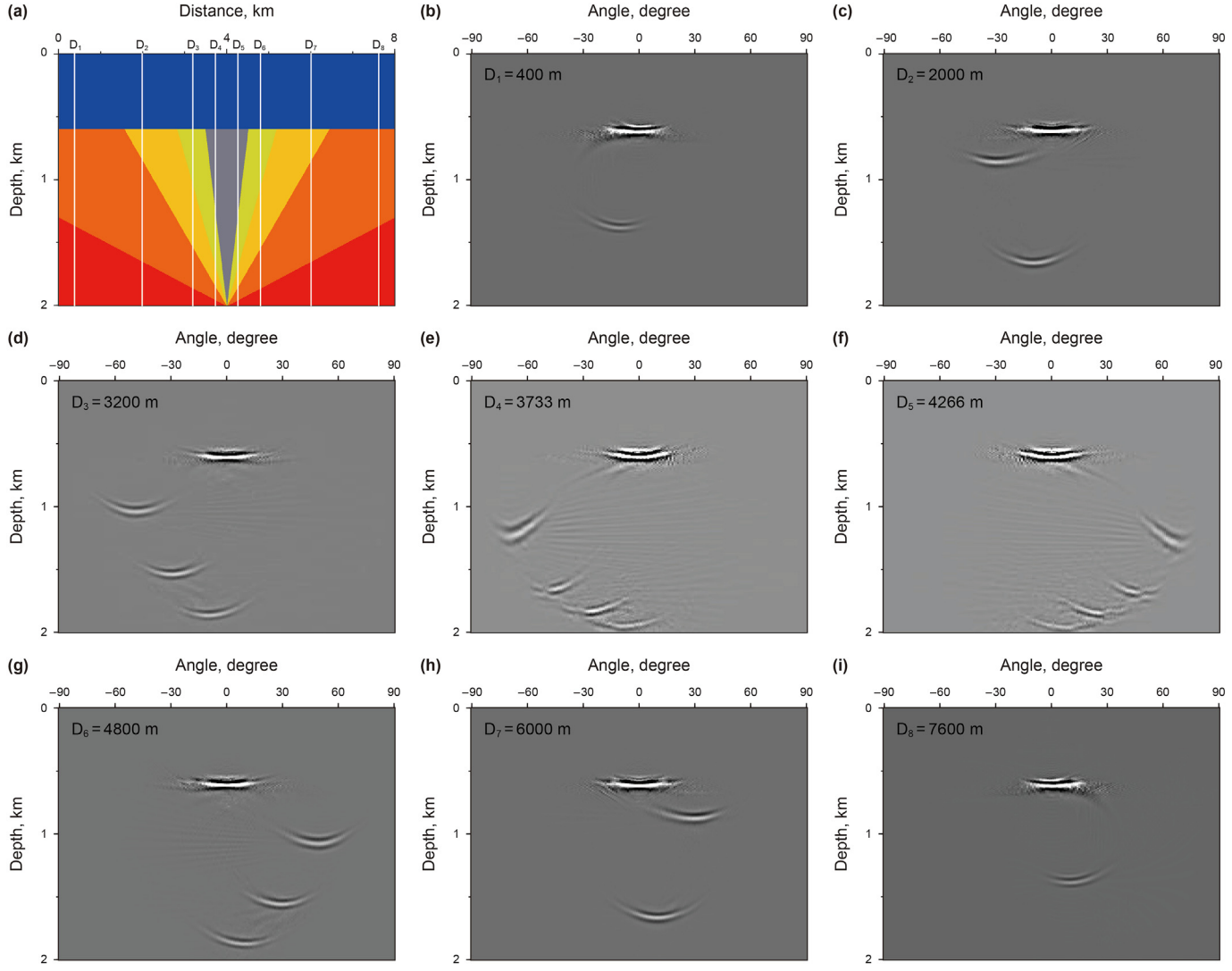

Fig. 6. The extraction results of DDCIGs of the light model: (**a**) velocity model, (**b**) DDCIGs at $D_1 = 400$ m, (**c**) DDCIGs at $D_2 = 2000$ m, (**d**) DDCIGs at $D_3 = 3200$ m, (**e**) DDCIGs at $D_4 = 3733$ m, (**f**) DDCIGs at $D_5 = 4266$ m, (**g**) DDCIGs at $D_6 = 4800$ m, (**h**) DDCIGs at $D_7 = 6000$ m, (**i**) DDCIGs at $D_8 = 7600$ m. White lines in the velocity model indicate locations for extraction, and here D means Distance.

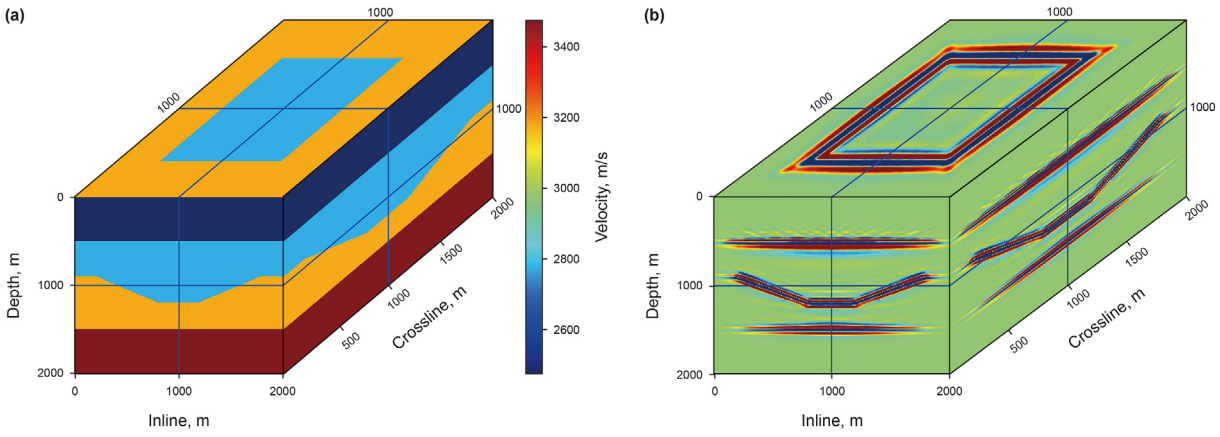

Fig. 7. 3D sag model and its migration result: (**a**) velocity model, (**b**) GBM result.

works better than Kirchhoff method (see Fig. 5c) in imaging steep structures.

Calculation of imaging results and the extraction of DDCIG are done simultaneously. We select eight positions from the final result, namely 400 m, 2000 m, 3200 m, 3733 m, 4266 m, 4800 m, 6000 m and 7600 m, respectively. Their corresponding dip-angle gathers are shown in Fig. 6.

As shown in Fig. 6, dip-angle gathers extracted at different positions have their own characteristics and are different from each other. These selected positions correspond to various connections that are equal or unequal between dip angles and the depth. Therefore, we can see that DDCIG has the ability to independently describe the characteristics of the data under the reference of dip angle and the depth. Specifically, eight gathers of Fig. 6b–i can be divided into two categories of Fig. 6b–e and Fig. 6f–i. These underground dip angles of Fig. 6b–e are all greater than 90° (here we set the increasing direction of the distance as the positive direction, that is, 0°, and the range of the dip angle is set from −90° to 90°). Accordingly, their imaging responses in the DDCIGs are also concentrated on the left area of −90°–0°. The latter case is completely opposite. It is a fact that the imaging response of the slanted layer in the DDCIG is similar to a curve with smiley shape of a stable phase vertex, and the angle corresponding to the stable phase vertex is equal to the dip angle of the slanted layer at the same depth when the migration velocity is completely correct (Kong et al., 2012). This can be clearly shown in Fig. 6d, g.

The light model is just a two-dimensional slanted layer model. In this section, we use it to highlight the characteristic and the application advantages of DDCIG. The second example is a three-dimensional sag model which is divided into four layers (see Fig. 7a). The first and last are horizontal layers, the central area between the second and third layers is designed as a large sag part, which is similar in shape to a basin in geology. Then, we also use the staggered-grid finite-difference method in the three-dimensional

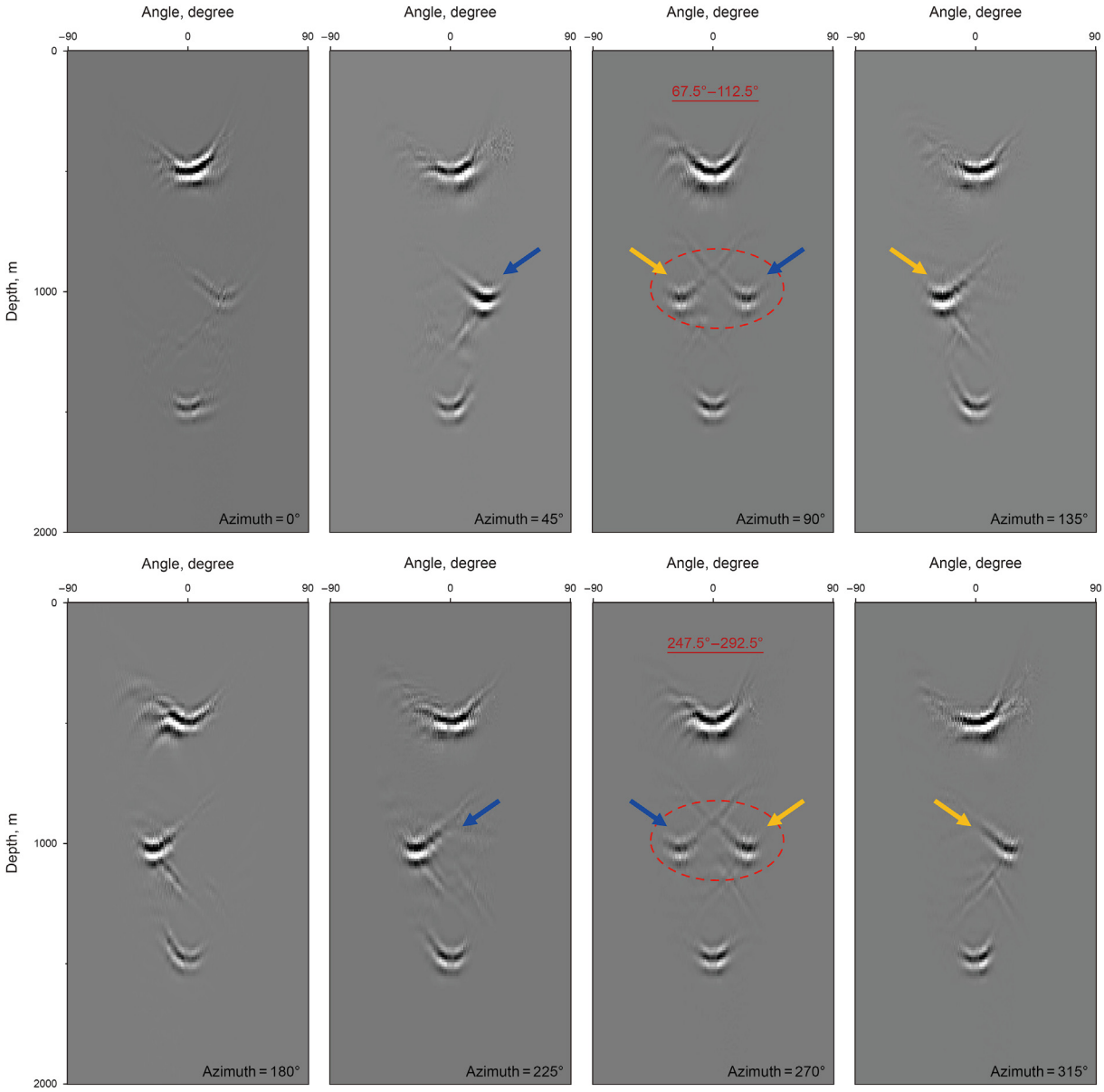

Fig. 8. The extraction results of eight-azimuth DDCIGs of Inline equals 900 m and Crossline equals 1500 m in the 3D sag model. The red number indicate the range of azimuth in the extracted gather.

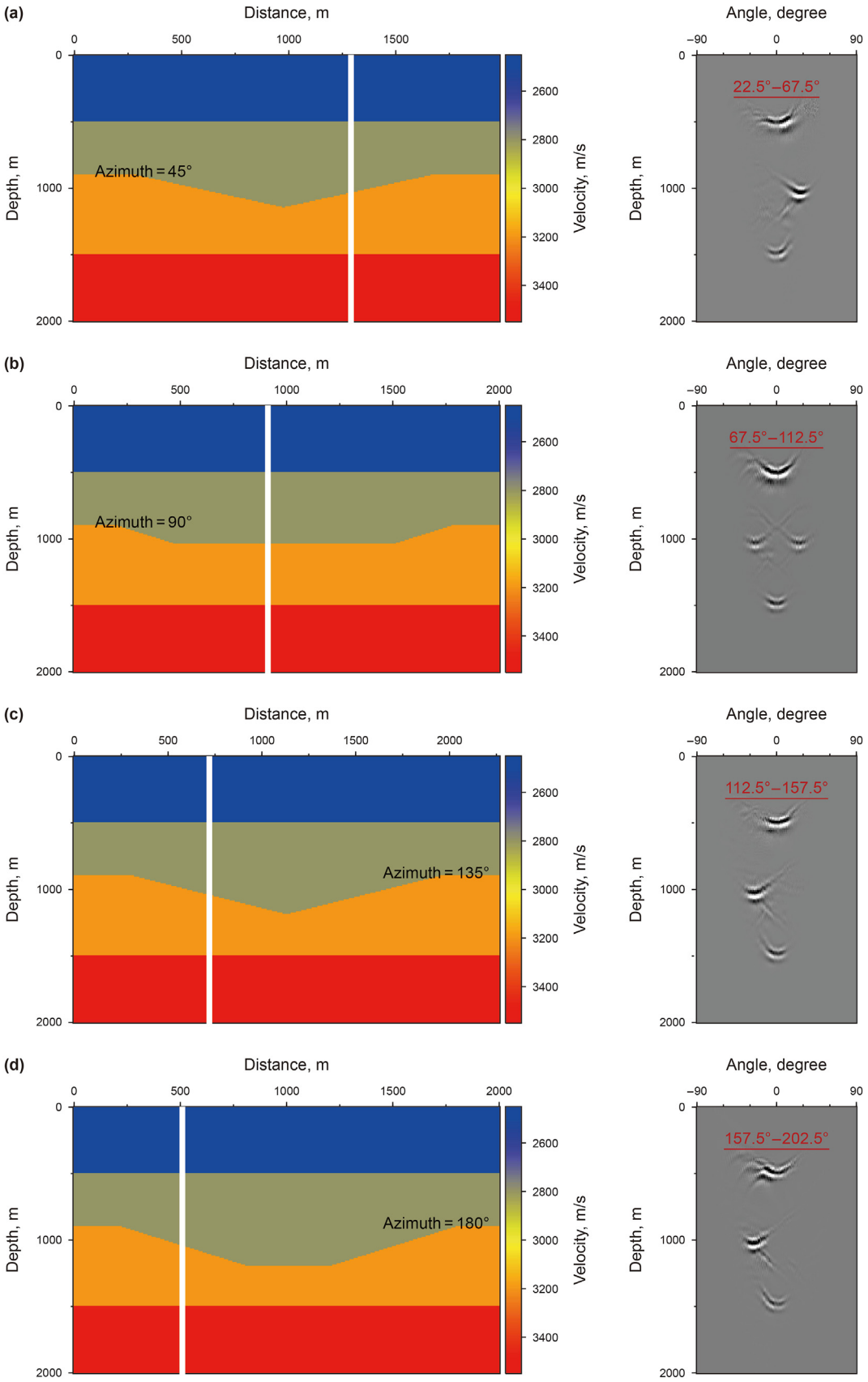

Fig. 9. Cutaways of the 3D sag model at Inline equals 900 m and Crossline equals 1500 m under different azimuths and results of DDCIGs: (**a**) azimuth is 45°, (**b**) azimuth is 90°, (**c**) azimuth is 135°, (**d**) azimuth is 180°. White lines indicate locations for extraction, and the red number indicate the range of azimuth.

numerical simulation. A total of 10 × 10 shots are simulated with a shot interval of 200 m in both vertical and horizontal direction. Meanwhile, 101 × 101 geophones are used for reception with an interval of 20 m in both vertical and horizontal direction as well. Significantly, the aspect ratio of the observation system has reached 1:1, which meets the requirement of wide-azimuth acquisition.

The obtained seismic record and the background velocity after Gaussian smoothing are used as input. 3D GBM result (see Fig. 7b) output below clearly portrays the potential of our method to describe events with accurate imaging position. The method of using Gaussian beam operator to image the subsurface has many advantages such as high efficiency and natural adaptability to steep structure imaging. Combination of our proposed technique with 3D GBM and simultaneous extraction of 3D DDCIGs during the data migration process is achieved.

As shown in Fig. 8, it is the eight-azimuth DDCIGs extracted from the position of Inline equals 900 m and Crossline equals 1500 m in the above three-dimensional sag model. The eight-azimuth refers to eight azimuths range from 0° to 315° at an interval of 45°. According to the theory of this paper, we can extract omnidirectional gathers in the dip-angle domain. However, the following three points must be considered: (1) limited storage space. By a simple calculation, all omnidirectional gathers of one point on the surface of the 3D model mentioned above requires approximately 49.96 MB and the model has 40,401 such points in total. If all of them are extracted for selection, 1.93 TB of storage space is required, which is obviously undesirable; (2) if eight azimuths are selected separately from the whole gather, it can be postulated that most gathers will be affected by low-frequency interference at different angles resulting in poor imaging quality; (3) the underground structure has media continuity, that is, the dip angle property of adjacent azimuths at the same imaging point changes gradually. Therefore, we can choose to stack several gathers in a certain range of angles for joint presentation. Finally, eight azimuths of DDCIGs in this paper are all the results of gather stack within the range of 22.5° on the left and right sides of the azimuth. The purpose is to fully describe the underground dip angle at the point.

Under this strategy, our final presentation is different from previous conventional results. As shown in Fig. 8, two curve responses co-exist at the same depth in one gather, such as 90° gather and 270° gather (see red circle). Take the 90° gather as an example, we can infer that the response on the left side is a high-azimuth effect from 90° to 112.5° by referring to the adjacent higher-azimuth 135° gather (see yellow arrow). Meanwhile, the response on the right side is a low-azimuth effect from 67.5° to 90° (see blue arrow). As a result, by comparing the difference of the response energy and stable phase vertex positions, we can infer the changing trend of the dip angle near each azimuth.

Cutaways of the three-dimensional sag model taken at Inline equals 900 m and Crossline equals 1500 m at four azimuths with their corresponding DDCIGs are shown in Fig. 9.

The combination of Figs. 8 and 9 proves the accuracy of the 3D DDCIG extraction method proposed in this paper. Also it highlights the application advantages such as detailed description of subsurface structural characteristics of the point imaged and the technique is not limited to a receiver line since it's omnidirectional. This has the advantage of being able to achieve accurate spatial imaging results at the lowest cost in the shortest time (compared to multiple two-dimensional seismic prospecting in the same exploration area). For example, according to the responses to the target layer under different azimuths in Fig. 8, it is possible to construct several cutaways shown in Fig. 9, and gain familiarity with structural characteristics near the imaging point.

In addition to its ability of distinguish different types of reflection energy, DDCIGs also have great advantages in the identification of diffraction energy. The third model is the three-dimensional diffraction model, which is used to test the identification ability of the extraction method for small-scale diffraction objects in this paper. As shown in Fig. 10a, it has four layers with the first and last layer horizontal and a curved boundary in between the second layer and third layer. There is a row of diffraction points above the layer and there are two rows below it. The difference between these points is that the upper one is relatively high-speed, and the lower one is relatively low-speed. So that we can test whether the responses of these diffraction points are different.

Using the same processing flow of the 3D sag model, GBM result of the 3D diffraction model can be finally obtained (see Fig. 10b). In this figure, events of layers are clear and characteristics of small-scale diffraction objects are obvious. To different types of diffraction points mentioned above, 3D GBM can achieve all accurate imaging results. In addition to the energy difference caused by the depth, different diffraction points can also have polarity reversals in the imaging response. Fig. 11 is the result of DDCIGs extracted during the migration process and the selected position is Inline equals 1000 m and Crossline equals 1200 m. In order to distinguish the difference between the reflection energy and the diffraction energy in the DDCIG, we choose to perform two different gain parameters on the same gather specially, which are “perc” equals 99.97 in Fig. 11a and “perc” equals 97.80 in Fig. 11b.

As shown in Fig. 11a, combining with the introduction above, we know that the response of the reflection layer at the DDCIG is an

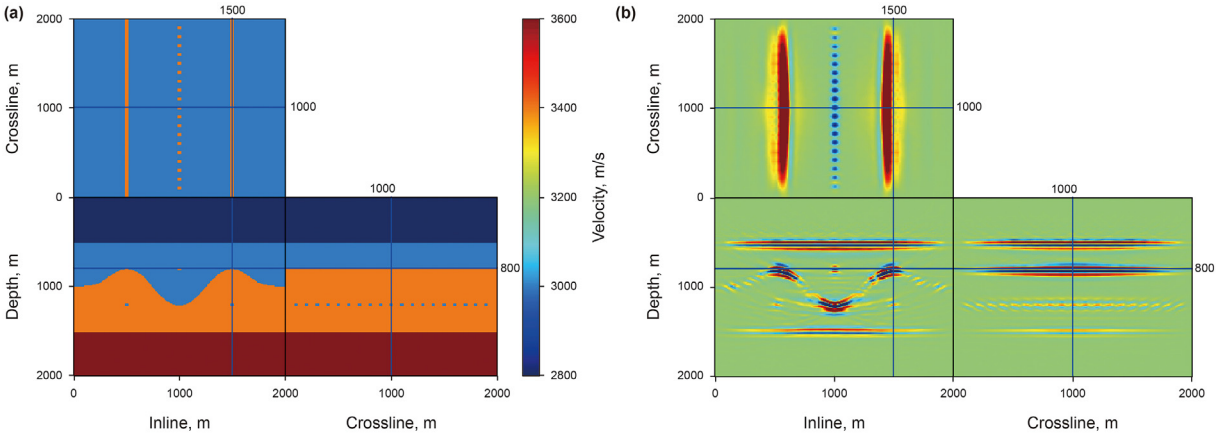

Fig. 10. 3D diffraction model and its migration result: (**a**) velocity model, (**b**) GBM result.

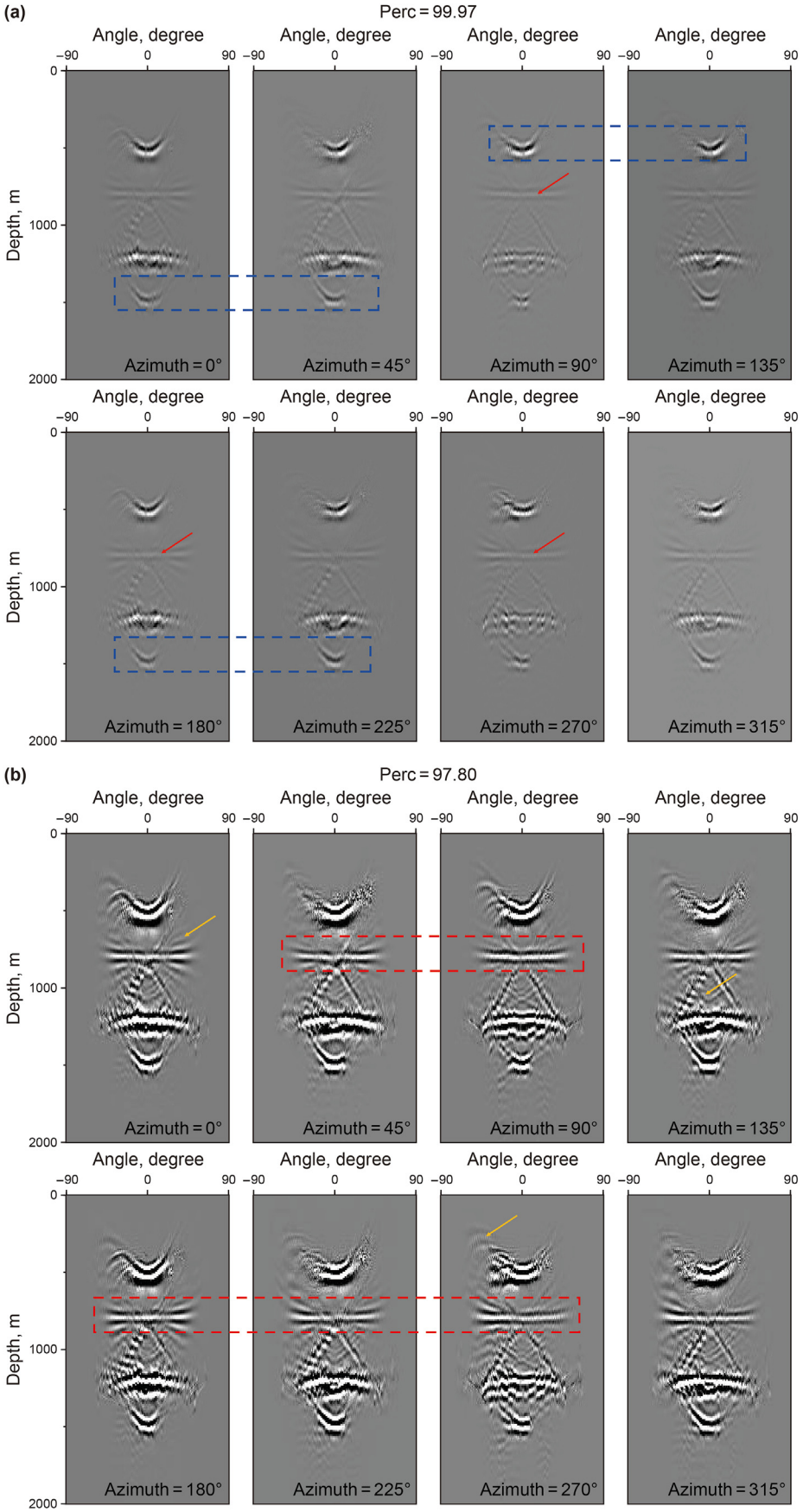

Fig. 11. The extraction results of eight-azimuth DDCIGs of Inline equals 1000 m and Crossline equals 1200 m in the 3D diffraction model: (**a**) perc equals 99.97, (**b**) perc equals 97.80.

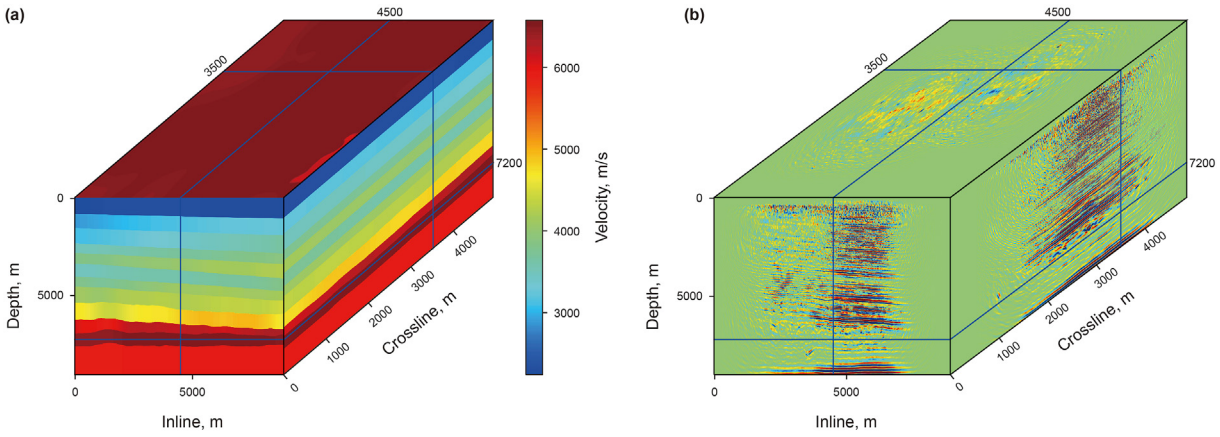

Fig. 12. 3D land data and its migration result: (**a**)velocity model, (**b**) GBM result.

upward opening curve with smiley shape (see blue box). As for the diffraction energy, it is known that the diffraction event in the DDCIG extracted directly above the diffraction point is horizontally linear (see red arrow). In order to suppress the reflection energy appropriately and highlight the diffraction energy in Fig. 11a, we adjust the gain parameter to portray clearer diffraction events (see red box) in Fig. 11b. It is worth noting that adjustment of the gain parameter results in reflection energy suppression and enhancement of low-frequency interference (see yellow arrow), but it does not affect subsequent processing. Compared with diffraction information, the interference is messy and distributed mainly in the edge area of main events. In summary, the ability of 3D-DDCIG to recognize small-scale diffraction objects has been tested and validated.

Finally, 3D DDCIG technique is applied on a field land data set from eastern China to verify the feasibility of its industrial applicability. Fig. 12a is the background velocity model constructed by the traditional ray tomography method, and Fig. 12b is the result after performing the 3D GBM.

The procedure was repeated and 3D-DDCIGs extracted below (see Fig. 13) shows results of three gathers with the azimuth of 90° at Inline equals 6600 m and Crossline equals 2500 m, the azimuth of 90° at Inline equals 3900 m and Crossline equals 2500 m, and the azimuth of 315° at Inline equals 4100 m and Crossline equals 3800 m. As shown in Fig. 13, red boxes mark several places with obvious reflection responses, and the weaker diffraction response, that is, the linear event can be seen in the place marked by the blue arrow. The suggested three reasons explain why the diffraction response is not

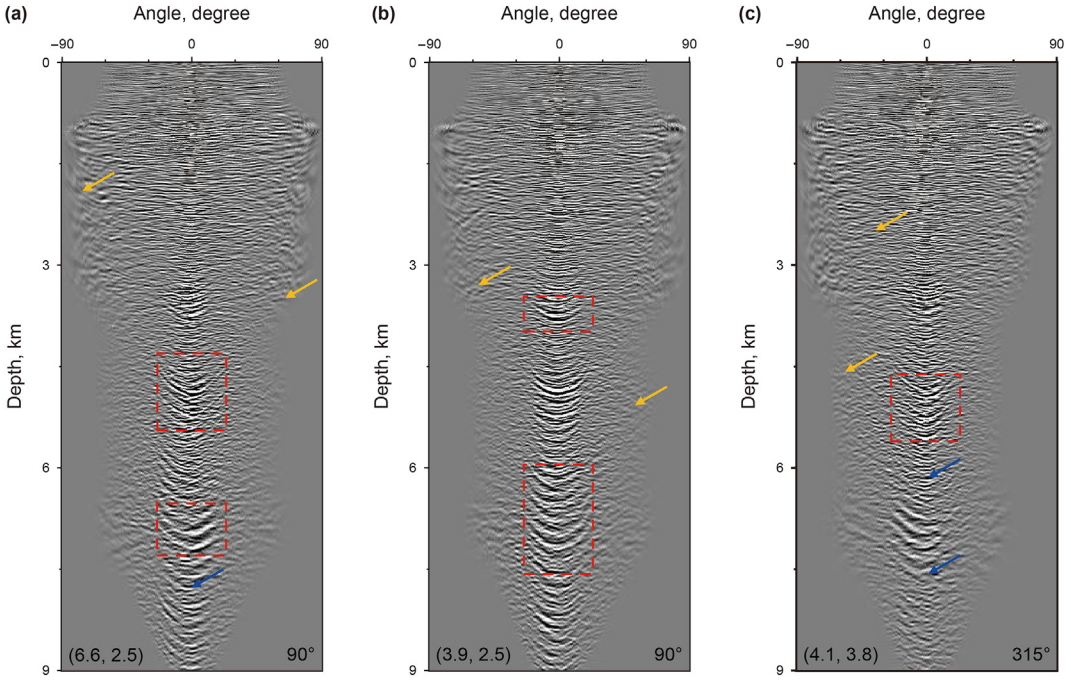

Fig. 13. The extraction results of DDCIGs at different positions of 3D land data. The numbers in the lower left corner indicate position coordinates, corresponding to inline and crossline respectively, the unit is km; the numbers in the lower right corner indicate azimuth.

very prominent: (1) the interference of the low-frequency noise from the actual data is serious (see yellow arrow); (2) the energy of seismic wave is seriously attenuated by absorption of the media when it propagates deep; (3) there are many underground reflection layers, so the reflection energy is strong and the diffraction energy is submerged in it. However, the diffraction energy can be extracted for imaging individually by some separation ways such as median filtering and hybrid Radon transform (Fomel et al., 2007; Bai et al., 2011; Klokov and Fomel, 2012).

4. Discussion

In this section, we will further discuss our method from three aspects of computational efficiency, industrialization advantages and application recommendations.

First and foremost, it is necessary to point out that our method of extraction is based on Gaussian beam operator, and it has a great efficiency advantage in theory. But in the migration of 3D land data, the efficiency advantage of 3D GBM is far less obvious than that of 2D GBM, compared with the same type of wave equation method. The main reason for this is that we select a full-coverage high-density ray tracing strategy algorithmically. Rays from sources and receivers are omnidirectional and at small intervals with multiple coverage for all imaging points. The benefits of it include: (1) it can guarantee high imaging accuracy; (2) even if it is extended to the target-oriented imaging, it will not affect the imaging quality; (3) true three-dimensional ray tracing can eliminate imaging artifacts of lateral waves. In addition, considering the optimization of the computational efficiency, it is possible for us to develop our method to the variable grid based on the coarse grid algorithm of Hale (1992a) and the irregular grid algorithm proposed by Popov et al. (2010). Moreover, we will replace the global scanning by the fast scanning strategy in the part of the realization of imaging conditions (Zhang et al., 2019).

It is necessary to balance calculation accuracy and efficiency in industrial production. In the imaging of 3D area, reverse time migration has higher imaging accuracy. But it has high requirements for memory space, calculation time and velocity dependence. Kirchhoff migration is currently a leading player in industry thanks to the superior computational efficiency advantages of ray-based methods. GBM is also a kind of ray-based method and owns the advantages of efficient imaging. Compared with Kirchhoff migration, it is more applicable and has no limitations of steep-structure imaging. Therefore, GBM is likely to replace Kirchhoff migration as the mainstream of industrial production in the future. At the same time, relying on the ability to distinguish the differential response to various signals such as reflection, diffraction and noise interference, 3D DDCIG is widely used in the fields of scattering-wave separation and imaging. It also provides an important tool for the identification of small-scale holes and cracks (Klokov and Fomel, 2012).

We should be careful about the following aspects when using the technique in industrial applications: (1) separation of diffraction based on 3D DDCIG needs to consider more azimuth information to avoid interference from reflection layers under certain azimuths; (2) if it is necessary to extract the attribute characteristics of the target area near a certain azimuth, set the range and interval of azimuths in the program and perform sub-azimuth imaging to highlight the imaging contribution under that azimuth.

5. Conclusions

By using 3D Gaussian beam operator that carries angle information, we have developed a method of 3D DDCIG extraction based on GBM. This method can be used in the field of diffraction identification, wavefield separation of reflection and diffraction, diffraction imaging and seismic attribute analysis in 3D media. Beginning with the mathematical and physical meaning of Gaussian beam operator, we obtain the representation of the ray vector after detailed analysis. Based on the complicated geometric relationship in the 3D local space near the imaging point, we derive two different kinds of DDCIG extraction formulas. The first example demonstrates that DDCIG has an obvious ability to distinguish reflection layers with different dip angles. The second and third examples show that our method can successfully identify the energy of reflection layers and diffraction targets in 3D media. The example of field data processing further confirms the conclusions obtained from the previous examples and shows its practical application capabilities. Therefore, our proposed method for extracting 3D DDCIG provides an effective and flexible tool for 3D data processing.

Acknowledgements

We are thankful to three anonymous reviewers for the valuable comments and suggestions that helped to improve this manuscript. The authors greatly appreciate the financial support jointly provided by the National Key R&D Program of China under contract number 2019YFC0605503C, the Major Projects during the 14th Five-year Plan period under contract number 2021QNLM020001, the National Outstanding Youth Science Foundation under contract number 41922028, the Funds for Creative Research Groups of China under contract number 41821002 and the Major Projects of CNPC under contract number ZD2019-183-003.

Appendix 1. Derivation of azimuth formula

In this appendix, we derive the formula of the azimuth in the three-dimensional local space. In order to explain the relationship between angles of the local space more clearly, we highlight several vectors on the basis of Fig. 2.

As shown in Fig. 14, we can reconstruct the process of reflection with the help of $\mathbf{a_s}$ and $\mathbf{a_r}$. Take case a as an example, $\mathbf{a}' = \mathbf{a_s} - \mathbf{a_r}$ and $\mathbf{a} = \mathbf{a_s} + \mathbf{a_r}$ are perpendicular to each other on the common plane κ (see Fig. 3). The straight line SR represents the intersection of the reflection plane η and the common plane κ, and the $\mathbf{a}'$ on it is exactly the same as the $\mathbf{a}'$ mentioned before. $\mathbf{n} = (1, 0, 0)$ is the reference direction vector we agreed before as well.

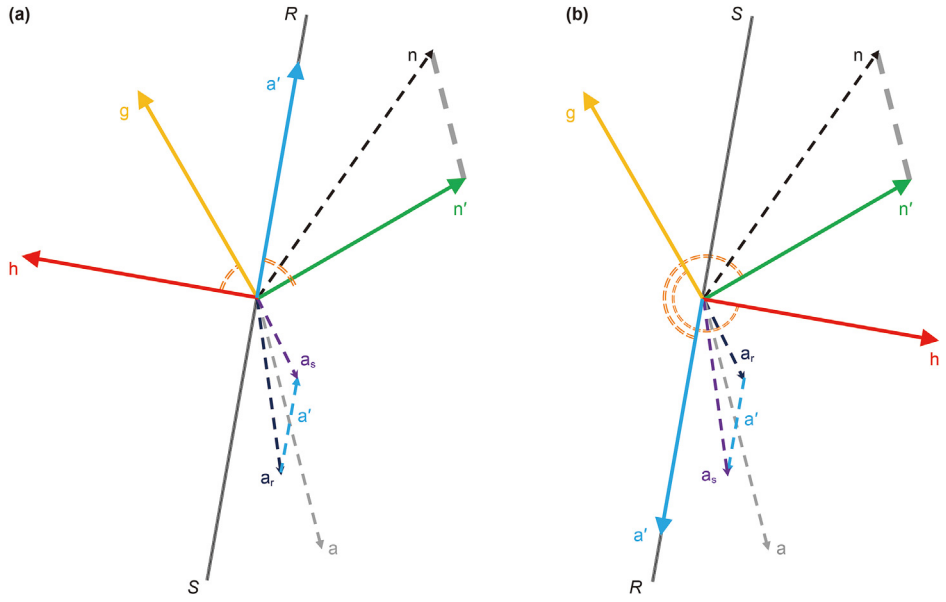

Fig. 14. Sketch of the reflection plane: (**a**) azimuth ranges from 0° to 180°, (**b**) azimuth ranges from 180° to 360°. The orange mark represents the azimuth.

To represent the azimuth conveniently, we transform the study plane from the horizontal plane to the reflection plane. After making the projection vector **n**' of the reference vector **n** on the reflection plane, the azimuth is the angle between **a**' and **n**' (see orange marks in Fig. 14). However, the mathematical expression of **n**' depends on the reflection plane η, and it is very difficult to solve it directly, so we need to convert it again. That is, make the vertical vectors of **a**' and **n**' respectively, and the angle between the two is the one we need. There is a key message that the vector **a** coincides with the normal line. According to the property that normal line is perpendicular to the reflection plane, **a** is also perpendicular to it. Thus, the vector **g** which is perpendicular to **n**' can be represented as $\mathbf{g} = \mathbf{n}' \times \mathbf{a} = \mathbf{n} \times \mathbf{a}$; Similarly, the vector **h** which is perpendicular to **a**' can be represented as $\mathbf{h} = \mathbf{a}' \times \mathbf{a} = \mathbf{a_s} \times \mathbf{a_r}$. What's more, according to the right-hand rule, the relative directions of vertical vectors are the same that are all counterclockwise vertical. In summary, the azimuth can be represented as the angle between the vector **g** and the vector **h**. So we can get

$$\cos(\beta) = \frac{\mathbf{g}\cdot\mathbf{h}}{|\mathbf{g}|\cdot|\mathbf{h}|} = \frac{(\mathbf{n}\times\mathbf{a})\cdot(\mathbf{a_s}\times\mathbf{a_r})}{|\mathbf{n}\times\mathbf{a}|\cdot|\mathbf{a_s}\times\mathbf{a_r}|}. \tag{17}$$

The sine function is also required because of the characteristic of the inverse trigonometric function that it is impossible to represent directions from 0° to 360° separately. So we need

$$\sin(\beta) = \frac{|\mathbf{h}\times\mathbf{g}|}{|\mathbf{h}|\cdot|\mathbf{g}|} = \frac{1}{|\mathbf{h}|\cdot|\mathbf{g}|}\cdot\frac{\mathbf{h}\times\mathbf{g}\cdot\mathbf{a}}{|\mathbf{a}|} = \frac{(\mathbf{a_s}\times\mathbf{a_r})\times(\mathbf{n}\times\mathbf{a})\cdot\mathbf{a}}{|\mathbf{a_s}\times\mathbf{a_r}|\cdot|\mathbf{n}\times\mathbf{a}|\cdot|\mathbf{a}|}, \tag{18}$$

here, in order to reduce the amount of calculation, we use the scalar product of the unit vector in the same direction to replace the calculation of vector modulus. The advantage of this is that it can improve calculation accuracy by avoiding multiple rounding errors, with improving the calculation efficiency at the same time.

References

Alkhalifah, T., 1995. Gaussian beam depth migration for anisotropic media. Geophysics 60 (5), 1474–1484. https://doi.org/10.1190/1.1443881.
Babich, V.M., Popov, M.M., 1989. Gaussian summation method (review). Radiophys. Quantum Electron. 32 (12), 1063–1081. https://doi.org/10.1007/bf01038632.
Bai, Y., Sun, Z., Chen, L., et al., 2011. Seismic diffraction separation in 2D and 3D space. In: 73rd Annual International Meeting, EAGE, Extended Abstracts. https://doi.org/10.3997/2214-4609.20148994.
Bleistein, N., 1999. Hagedoorn told us how to do Kirchhoff migration and inversion. Lead. Edge 18 (8), 918–927. https://doi.org/10.1190/1.1438407.
Brandsberg-Dahl, S., de Hoop, M.V., Ursin, B., 2003. Focusing in dip and AVA compensation on scattering-angle/azimuth common image gathers. Geophysics 68 (1), 232–254. https://doi.org/10.1190/1.1543210.
Cai, J., Fang, W., Wang, H., 2013. Azimuth–opening angle domain imaging in 3D Gaussian beam depth migration. J. Geophys. Eng. 10 (2), 025013. https://doi.org/10.1088/1742-2132/10/2/025013.
Červený, V., 1972. Seismic rays and ray intensities in inhomogeneous anisotropic media. Geophys. J. Int. 29 (1), 1–13. https://doi.org/10.1111/j.1365-246x.1972.tb06147.x.
Červený, V., Popov, M.M., Pšenčík, I., 1982. Computation of wave fields in inhomogeneous media – Gaussian beam approach. Geophys. J. Int. 70 (1), 109–128. https://doi.org/10.1111/j.1365-246x.1982.tb06394.x.
Červený, V., 1983. Synthetic body wave seismograms for laterally varying layered structures by the Gaussian beam method. Geophys. J. Int. 73 (2), 389–426. https://doi.org/10.1111/j.1365-246x.1983.tb03322.x.
Červený, V., Pšenčík, I., 1983b. Gaussian beams and paraxial ray approximation in three-dimensional elastic inhomogeneous media. J. Geophys. 53, 1–15.
Červený, V., Pšenčík, I., 1983c. Gaussian beams in two-dimensional elastic inhomogeneous media. Geophys. J. Int. 72 (2), 417–433. https://doi.org/10.1111/j.1365-246X.1983.tb03793.x.
Červený, V., Pšenčík, I., 1984. Gaussian beams in elastic 2-D laterally varying layered structures. Geophys. J. Int. 78 (1), 65–91. https://doi.org/10.1111/j.1365-246x.1984.tb06472.x.
Červený, V., 2005. Seismic Ray Theory. Cambridge University Press, New York.
Claerbout, J.F., 1970. Coarse grid calculations of waves in inhomogeneous media with applications to delineation of complicated seismic structure. Geophysics 35 (3), 407–418. https://doi.org/10.1190/1.1440103.
Duan, P., Cheng, J., Chen, A., et al., 2013. Local angle-domain Gaussian beam prestack depth migration in a TI medium. Chin. J. Geophys. 56 (12), 4206–4214. https://doi.org/10.6038/cjg20131223 **(in Chinese)**.
Fomel, S., Landa, E., Taner, M.T., 2007. Poststack velocity analysis by separation and imaging of seismic diffractions. Geophysics 72 (6), U89–U94. https://doi.org/10.1190/1.2781533.
Geng, Y., Wu, R., Gao, J., 2011. Efficient Gaussian packets representation and seismic imaging. In: 81st Annual International Meeting. SEG, pp. 3398–3403. https://doi.org/10.1190/1.3627903 expanded abstracts.
Geng, Y., Wu, R., Gao, J., 2014. Gabor-frame-based Gaussian packet migration. Geophys. Prospect. 62 (6), 1432–1452. https://doi.org/10.1111/1365-2478.12152.
Gray, S.H., Notfors, C., Bleistein, N., 2002. Imaging using multi-arrivals: Gaussian beams or multi-arrival Kirchhoff?. In: 72nd Annual International Meeting. SEG, expanded abstracts, pp. 1117–1120. https://doi.org/10.1190/1.1816843.
Gray, S.H., 2005. Gaussian beam migration of common-shot records. Geophysics 70

(4), S71–S77. https://doi.org/10.1190/1.1988186.
Gray, S.H., 2007. Angle gathers for Gaussian beam migration. In: 69th Annual International Meeting, EAGE, Extended Abstracts. https://doi.org/10.3997/2214-4609.201401519.
Gray, S.H., Bleistein, N., 2009. True-amplitude Gaussian-beam migration. Geophysics 74 (2), S11–S23. https://doi.org/10.1190/1.3052116.
Hale, D., 1992a. Computational Aspects of Gaussian Beam Migration, vol. 139. Colorado School of Mines Center for Wave Phenomena Report. https://doi.org/10.2172/10167616.
Hale, D., 1992b. Migration by the Kirchhoff, Slant Stack, and Gaussian Beam Methods, vol. 121. Colorado School of Mines Center for Wave Phenomena Report. https://doi.org/10.2172/10167620.
Han, J., Wang, Y., Xing, Z., et al., 2014. Gaussian beam prestack depth migration of converted wave in TI media. J. Appl. Geophys. 109, 7–14. https://doi.org/10.1016/j.jappgeo.2014.07.008.
Hill, N.R., 1990. Gaussian beam migration. Geophysics 55 (11), 1416–1428. https://doi.org/10.1190/1.1442788.
Hill, N.R., 2001. Prestack Gaussian-beam depth migration. Geophysics 66 (4), 1240–1250. https://doi.org/10.1190/1.1487071.
Huang, J., Yang, J., Li, Z., et al., 2016. An amplitude-preserved Gaussian beam migration based on wave field approximation in effective vicinity under irregular topographical conditions. Chin. J. Geophys. 59 (6), 2245–2256. https://doi.org/10.6038/cjg20160627 **(in Chinese)**.
Huang, L.J., Fehler, M.C., 2000. Globally optimized fourier finite-difference migration method. In: 70th Annual International Meeting. SEG, pp. 802–805. https://doi.org/10.1190/1.1816192 expanded abstracts.
Jiang, W., Liu, Z., Zhang, J., 2017. Diffraction imaging using reverse time migration with poynting vectors. In: 87th Annual International Meeting. SEG, pp. 1028–1032. https://doi.org/10.1190/segam2017-17683099.1 expanded abstracts.
Kachalov, A.P., Popov, M.M., 1981. Application of the method of summation of Gaussian beams for calculation of high-frequency wave fields. Sov. Phys. Dokl. 26, 604–606.
Klokov, A., Fomel, S., 2012. Separation and imaging of seismic diffractions using migrated dip-angle gathers. Geophysics 77 (6), S131–S143. https://doi.org/10.1190/geo2012-0017.1.
Kong, X., Li, Z., Huang, J., et al., 2012. Diffracting objective imaging based on plane wave record. Oil Geophys. Prospect. 47 (4), 674–681. https://doi.org/10.13810/j.cnki.issn.1000-7210.2012.04.014 **(in Chinese)**.
Kong, X., Li, Z., Li, C., et al., 2016. Diffraction separation in dip-angle domain based on Gaussian beam migration. J China Univ Pet: Ed Nat Sci. 40 (1), 49–55. https://doi.org/10.3969/j.issn.1673-5005.2016.01.007 **(in Chinese)**.
Kwangjin, Y., 2017. Reverse time migration angle gathers using Poynting vector and pseudospectral method. In: 87th Annual International Meeting. SEG, pp. 4630–4634. https://doi.org/10.1190/segam2017-17749395.1 expanded abstracts.
Liu, J., Palacharla, G., 2011. Multiarrival Kirchhoff beam migration. Geophysics 76 (5), WB109–WB118. https://doi.org/10.1190/geo2010-0403.1.
Liu, J., Xie, X., Chen, B., 2017. RTM amplitude correction in angle-domain based on Poynting vectors. In: 87th Annual International Meeting. SEG, pp. 95–98. https://doi.org/10.1190/IGC2017-025 expanded abstracts.
Nolan, C.J., Symes, W.W., 1996. Imaging and coherency in complex structures. In: 66th Annual International Meeting. SEG, expanded abstracts, pp. 359–362. https://doi.org/10.1190/1.1826642.
Nowack, R.L., Sen, M.K., Stoffa, P.L., 2003. Gaussian beam migration for sparse common-shot and common-receiver data. In: 73rd Annual International Meeting. SEG, pp. 1114–1117. https://doi.org/10.1190/1.1817470 expanded abstracts.
Nowack, R.L., 2008. Focused Gaussian beams for seismic imaging. In: 78th Annual International Meeting. SEG, pp. 2376–2380. https://doi.org/10.1190/1.3059356 expanded abstracts.
Nowack, R.L., 2011. Dynamically focused Gaussian beams for seismic imaging. Int. J. Geophys. 1–8. https://doi.org/10.1155/2011/316581.
Popov, M.M., 1982. A new method of computation of wave fields using Gaussian beams. Wave Motion 4 (1), 85–97. https://doi.org/10.1016/0165-2125(82)90016-6.
Popov, M.M., 2002. Ray theory and Gaussian beam method for geophysicists. Salvador: EDUFBA.
Popov, M.M., Semtchenok, N.M., Popov, P.M., et al., 2010. Depth migration by the Gaussian beam summation method. Geophysics 75 (2), S81–S93. https://doi.org/10.1190/1.3361651.
Shi, X., Sun, J., Sun, H., et al., 2016. The time-domain depth migration by the summation of delta packets. Chin. J. Geophys. 59 (7), 2641–2649. https://doi.org/10.6038/cjg20160727 **(in Chinese)**.
Thomas, A.D., Graham, A.W., 2011. RTM angle gathers using Poynting vectors. In: 81st Annual International Meeting. SEG, pp. 3109–3113. https://doi.org/10.1190/1.3627841 expanded abstracts.
Ursin, B., 2004. Parameter inversion and angle migration in anisotropic elastic media. Geophysics 69 (5), 1125–1142. https://doi.org/10.1190/1.1801931.
Xu, S., Chauris, H., Lambaré, G., et al., 2001. Common-angle migration: a strategy for imaging complex media. Geophysics 66 (6), 1877–1894. https://doi.org/10.1190/1.1487131.
Yang, J., Huang, J., Wang, X., et al., 2015a. An amplitude-preserved adaptive focused beam seismic migration method. Petrol. Sci. 12 (3), 417–427. https://doi.org/10.1007/s12182-015-0044-7.
Yang, J., Huang, J., Wang, X., et al., 2015b. Prestack Fresnel beam migration method under complex topographic conditions. Chin. J. Geophys. 58 (10), 3758–3770. https://doi.org/10.6038/cjg20151026 **(in Chinese)**.
Yang, J., Zhu, H., Huang, J., et al., 2018a. 2D isotropic elastic Gaussian beam migration for common-shot multicomponent records. Geophysics 83 (2), S127–S140. https://doi.org/10.1190/geo2017-0078.1.
Yang, J., Zhu, H., McMechan, G., et al., 2018b. Time-domain least-squares migration using the Gaussian beam summation method. Geophys. J. Int. 214 (1), 548–572. https://doi.org/10.1093/gji/ggy142.
Yao, G., da Silva, N.V., Wu, D., 2019. Reflection-waveform inversion regularized with structure-oriented smoothing shaping. Pure Appl. Geophys. 12, 5315–5335. https://doi.org/10.1007/s00024-019-02265-6.
Yao, G., Wu, D., Wang, S., 2020. A review on reflection waveform inversion. Petrol. Sci. 17, 334–351. https://doi.org/10.1007/s12182-020-00431-3.
Yue, Y., Li, Z., Qian, Z., et al., 2012. Amplitude-preserved Gaussian beam migration under complex topographic conditions. Chin. J. Geophys. 55 (4), 1376–1383. https://doi.org/10.6038/j.issn.0001-5733.2012.04.033 **(in Chinese)**.
Yue, Y., Qian, Z., Zhang, X., et al., 2019a. Gaussian beam based Born modeling method for single-scattering waves in acoustic medium. Chin. J. Geophys. 62 (2), 648–656. https://doi.org/10.6038/cjg2019M0367 **(in Chinese)**.
Yue, Y., Sava, P., Qian, Z., et al., 2019b. Least-squares Gaussian beam migration in elastic media. Geophysics 84 (4), S329–S340. https://doi.org/10.1190/geo2018-0391.1.
Yue, Y., Sun, H., Wu, R., et al., 2020. Gaussian beam born modeling for single-scattering waves in visco-acoustic media. Geosci. Rem. Sens. Lett. IEEE 1–5. https://doi.org/10.1109/LGRS.2020.3015906.
Yue, Y., Liu, Y., Gray, S., 2021a. Accelerating least-squares Kirchhoff time migration using beam methodology. Geophysics 86 (3), S221–S234.
Yue, Y., Liu, Y., Li, Y., et al., 2021b. Least-squares Gaussian beam migration in viscoacoustic media. Geophysics 86 (1), S17–S28.
Žáček, K., 2004. Gaussian packet prestack depth migration. In: 74th Annual International Meeting. SEG, pp. 957–960. https://doi.org/10.1190/1.1845325 expanded abstracts.
Žáček, K., 2006. Decomposition of the wave field into optimized Gaussian packets. Studia Geophys. Geod. 50, 367–380. https://doi.org/10.1007/s11200-006-0023-y.
Zhang, R., Huang, J., Zhuang, S., et al., 2019. Target-oriented Gaussian beam migration using a modified ray tracing scheme. Petrol. Sci. 16, 1301–1319. https://doi.org/10.1007/s12182-019-00388-y.
Zhang, Y., Xu, S., Bleistein, N., et al., 2007. True-amplitude, angle-domain, common-image gathers from one-way wave-equation migrations. Geophysics 72 (1), S49–S58. https://doi.org/10.1190/1.2399371.
Zhu, T., Gray, S.H., Wang, D., 2007. Prestack Gaussian-beam depth migration in anisotropic media. Geophysics 72 (3), S133–S138. https://doi.org/10.1190/1.2711423.